J. Fluid Mech. (2014), *vol.* 744, *pp.* 65–88. © Cambridge University Press 2014
doi:10.1017/jfm.2014.71

Patterns of a creeping water-spout flow

Miguel Herrada[1,†] **and Vladimir Shtern**[2]

[1]E. S. I., Universidad de Sevilla, Camino de los Descubrimientos s/n 41092, Spain

[2]Shtern Research and Consulting, Houston, TX 77096, USA

(Received 24 September 2013; revised 8 January 2014; accepted 28 January 2014; first published online 10 March 2014)

This paper explains a mechanism of eddy formation in a slow air–water motion, driven by the rotating top disk, in a vertical sealed cylinder. The numerical simulations reveal nine changes in the flow topology as water volume fraction H_w varies from 0 to 1. At H_w around 0.8, there are two large regions of the clockwise meridional circulation, one in air and one in water. These regions are separated by two small cells of the anticlockwise circulation adjacent to the interface near the sidewall in water and near the axis in air. The air cell is a thin layer and topologically is a bubble–ring for $0.745 < H_w < 0.785$. Alterations of this flow pattern are explored as (i) pressure increases, (ii) the bottom disk co-rotates and (iii) the top-disk rotation speeds up. This paper provides the physical reasoning behind the flow transformations; the results are of fundamental interest and can be utilized in bioreactors.

Key words: multiphase flow, vortex dynamics, vortex flows

1. Introduction

A complicated pattern of a creeping flow is counterintuitive. It seems that the motion dominated by viscous diffusion should be topologically simple. For this reason, the discovery of a chain of eddies in a slow flow between two inclined planes (Moffatt 1964) has attracted much attention and initiated numerous studies of creeping cellular motions. In steady planar or axisymmetric flows, similar eddies have been found in a plane cavity (Moffatt 1964; Shankar & Deshpande 2000), cone (Wakiya 1976), cylinder (Blake 1979; Hills 2001), in cavities with oppositely moving walls (Gürcan *et al.* 2003; Wilson, Gaskell & Savage 2005), between concentric cones (Hall, Hills & Gilbert 2007) and coaxial cylinders (Shtern 2012*a*).

The physical reasoning behind the cellular pattern is determined by dead-end geometry and the dissipation of kinetic energy. The cavity's dead end yields a counterflow and the dissipation appears to be smaller in a set of eddies than that in a global counterflow. According to the Helmholtz theorem (Happel & Brenner 1965), the dissipation rate of kinetic energy in the Stokes flow is less than that in any other motion of an incompressible viscous fluid under the same boundary conditions. The cellular pattern provides minimal dissipation for the planar and axisymmetric flows.

Our paper reveals a different mechanism of the cell formation in a steady axisymmetric two-fluid rotating flow. This mechanism is kinematic and based on

† Email address for correspondence: herrada@us.es

https://doi.org/10.1017/jfm.2014.71 Published online by Cambridge University Press

the capability of swirl to generate the circulatory meridional motion. We explore how this mechanism works in a slow air–water flow driven by the rotating top disk in a sealed vertical cylinder.

Air–water circulatory flows have recently attracted the attention of researchers due to their applications in aerial bioreactors (Ramazanov *et al.* 2007). In cylindrical bioreactors, a rotating disk is typically used to induce both swirl and the meridional motions. Lo Jacono, Nazarinia & Brøns (2009) experimentally and Liow *et al.* (2009) numerically explored air–water flows in cylindrical containers. Lo Jacono *et al.* addressed a whirlpool-like flow where the rotating bottom disk pushes the interface down near the axis and up near the sidewall. Liow *et al.* investigated a water-spout-like flow, where the interface is deformed up near the axis and down near the sidewall by the rotating top disk, which helps transport air oxygen required for the efficient growth of tissue culture in water.

Recent numerical studies of two-fluid flows in a vertical sealed cylinder found a number of unusual features absent in one-fluid flows. Among them, the most surprising and potentially important for applications is the existence of thin circulation layers (TCLs) adjacent to the interface. There are local TCLs in the lower (Brady, Herman & Lopez 2012*a*,*b*) and upper (Herrada, Shtern & López-Herrera 2013*a*) fluids, if the bottom disk rotates, and a global TCL adjacent to the entire interface from below, if the top disk rotates (Herrada, Shtern & López-Herrera 2013*b*). These TCLs emerge as the rotation speeds up.

The surface-area-to-volume ratio of a TCL is larger than that of a bubble. This feature is beneficial for mass and heat transfer that can be utilized in applications, e.g. bioreactors. The tissue growth is a time-consuming process requiring a slow motion of ingredients and small shear stresses. Our paper shows that TCLs can occur in an extremely slow (creeping) flow as well. The kinematic mechanism of the TCL formation is explained below.

The centrifugal force, induced by the rotating top disk, pushes air to the periphery near the disk and thus generates the clockwise meridional circulation, resulting in the convergence of air toward the axis near the interface. The water meridional motion is driven by two factors, both provided by the air flow: (*a*) swirl and (*b*) meridional velocities at the interface.

Factors (*a*) and (*b*) tend to move water in opposite directions: the swirl (meridional) velocity drives the clockwise (anticlockwise) circulation. If the water volume fraction, H_w, is small, factor (*b*) dominates and the bulk circulation of water is anticlockwise. As H_w increases, factor (*a*) becomes stronger and induces a cell of the clockwise circulation near the bottom centre for $H_w > 0.64$.

Next, the clockwise (anticlockwise) circulation expands (shrinks) in water. As the water's clockwise circulation reaches air, it reverses the meridional velocity at the interface, v_t, which becomes positive. At $H_w = 0.8$, v_t is negative only in the sidewall vicinity where the anticlockwise circulation of water shrinks into a small cell (figure 11). In the air, the reversed v_t induces a layer of the anticlockwise circulation whose features are paradoxical. One striking feature is that this layer is very thin compared with the container dimension. This feature is due to the small air-to-water density ratio. Another striking feature is its unusual topology: the layer is a bubble–ring for $0.745 < H_w < 0.785$. Typically, the bubble–ring shape is intermediate between the bubble and ring shapes. Here, the bubble–ring TCL is robust because it is adjacent to the interface (see § 5.4 for more details). As H_w varies from 0 to 1, the flow undergoes nine (!) topological metamorphoses.

https://doi.org/10.1017/jfm.2014.71 Published online by Cambridge University Press

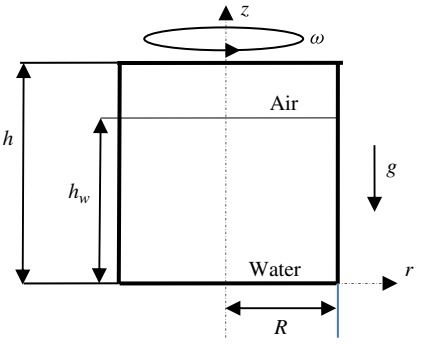


FIGURE 1. Schematic of the problem.

We also explore how the flow pattern varies as the air density rises. To this end, pressure inside the container is increased at the fixed (room) temperature. Next, the control effect of additional weak co-rotation of the bottom disk is explored. Finally, we study the effect of the increasing rotation of the top disk, i.e. of finite values of the Reynolds number, Re.

Thus, our paper reveals that the creeping water-spout flow is rich in intriguing and important features: (i) the multicell pattern, developed by competing effects of the swirl and meridional motions, (ii) the numerous topological metamorphoses as H_w varies, (iii) the TCL in the air and (iv) the robust bubble–ring (RBR) shape of this layer. This two-fluid motion is one more representative of paradoxical counterflows (Shtern 2012*b*).

In the rest of this paper, we formulate the problem in § 2, describe the numerical technique in § 3, explore the flow pattern for small H_w (§ 4), how the pattern changes as H_w increases (§ 5), the flow details at $H_w = 0.8$ (§ 6), the disappearance of air cells as H_w approaches one (§ 7), the effects of the increasing air-to-water density ratio (§ 8), bottom disk co-rotation (§ 9), Re (§ 10), summarize the results in § 11 and verify their grid independence in the Appendix.

2. Problem formulation

2.1. *Flow geometry*

Figure 1 is a problem schematic. The lower part, $0 < z < h_w$, of the cylindrical container is filled with water, the upper part, $h_w < z < h$, is filled with air; h is the cylinder height; $\boldsymbol{g}$ is the gravity acceleration. The interface is depicted by the thin horizontal line, $z = h_w$. The top disk (at $z = h$) rotates with angular velocity ω. The rotation strength can be characterized by the Reynolds number, $Re = \omega R^2/\nu_w$; R is the cylinder radius; and ν_w is the kinematic viscosity of water. The other control parameters are aspect ratio $H = h/R$ and the water volume fraction $H_w = h_w/h$. Since the aspect ratio of aerial bioreactors is typically close to one (Ramazanov *et al.* 2007; Liow *et al.* 2009), here $H = 1$ is fixed while H_w varies.

2.2. *Governing equations*

Using R, ωR and $\rho_w \omega^2 R^2$ as scales for length, velocity and pressure, respectively, renders all variables dimensionless. We consider steady axisymmetric flows of air and

https://doi.org/10.1017/jfm.2014.71 Published online by Cambridge University Press

water both governed by the Navier–Stokes equations for a viscous incompressible fluid (Batchelor 1967),

$$r^{-1}\partial(ru)/\partial r + \partial w/\partial z = 0, \tag{2.1}$$

$$u\partial u/\partial r + w\partial u/\partial z = v^2/r - \rho_n \partial p/\partial r + \nu_n Re^{-1}(\nabla^2 u - u/r^2), \tag{2.2}$$

$$u\partial v/\partial r + w\partial v/\partial z + uv/r = \nu_n Re^{-1}(\nabla^2 v - v/r^2), \tag{2.3}$$

$$u\partial w/\partial r + w\partial w/\partial z = -\rho_n \partial p/\partial z + \nu_n Re^{-1}(\nabla^2 w), \tag{2.4}$$

where $\nabla^2 \equiv r^{-1}\partial(r\partial/\partial r)/\partial r + \partial^2/\partial z^2$, (u, v, w) are the velocity components in the cylindrical coordinates (r, ϕ, z) and p is pressure reduced by the hydrostatic contribution. The coefficients, ρ_n and ν_n, are both equal to 1 at $n = 1$ (in water) while $\rho_n = \rho_w/\rho_a$ and $\nu_n = \nu_a/\nu_w$ at $n = 2$ (in air); $\nu_w = 10^{-6}$ m^2 s^{-1} and $\nu_a = 15 \times 10^{-6}$ m^2 s^{-1} are the kinematic viscosities; $\rho_w = 1000$ kg m^{-3} and $\rho_a = 1.22$ kg m^{-3} are the densities; subscripts 'a' and 'w' denote 'air' and 'water'. This air density value corresponds to the atmospheric pressure and the room temperature.

2.3. *Boundary conditions*

Equations (2.1)–(2.4) are solved under the following boundary conditions.

(i) Regularity at the axis, $0 < z < H$, $r = 0$: $u = v = 0$, $\partial w/\partial r = 0$.

(ii) No-slip at the walls: $u = v = w = 0$ at the still disk, $0 < r < 1$, $z = 0$, and at the sidewall, $0 < z < H$, $r = 1$; $u = w = 0$, $v = r$ at the rotating disk, $0 < r < 1$, $z = H$.

(iii) Continuity of all of the velocity and stress components at the air–water interface, $z = F(r)$. In particular, the balance for the normal stresses yields that

$$p_w - p_a = We^{-1}\nabla \cdot \boldsymbol{n} - Re^{-1}\boldsymbol{n} \cdot (\tau_w - \mu_r \tau_a) \cdot \boldsymbol{n} - Fr^{-1}(1 - \rho_a/\rho_w)z + C \tag{2.5}$$

where $We = \rho_w \omega^2 R^3/\sigma$ is the Weber number, characterizing the effect of surface tension σ at the interface; $Fr = \omega^2 R/g$ is the Froude number, which is a centrifugal-to-gravity acceleration ratio, $g = 9.81$ m^2 s^{-1} is the gravity acceleration magnitude (figure 1); $\boldsymbol{n}$ is the unit vector normal to the interface; τ_w and τ_a are tensors of the viscous stresses in water and air, respectively; μ_r is the air-to-water ratio of the dynamic viscosities; C is a constant which is determined by imposing the mass conservation of the liquid inside the container as the interface is deformed,

$$2\int_0^1 F(r) r \, \mathrm{d}r = H_w. \tag{2.6}$$

2.4. *Reduced problem*

As $Re \to 0$, the motion becomes very slow and the interface deformation becomes negligible, $F(r) \equiv H_w$. The nonlinear terms become negligibly small compared with the linear terms in (2.3), which reduces to

$$\nabla^2 v - v/r^2 = 0. \tag{2.7}$$

This equation has a non-zero solution due to the boundary condition at the top disk: $v = r$ at $z = H$. At all other walls the swirl velocity is zero, v = 0. At the interface, v and the swirl shear stresses are continuous: $v_w = v_a$ and $\partial v_w/\partial z = \mu_r \partial v_a/\partial z$ at $z = H_w$. Thus the problem for the swirl velocity becomes separated from the problem for

https://doi.org/10.1017/jfm.2014.71 Published online by Cambridge University Press

the meridional motion in the limiting case as $Re \to 0$, similar to that in the one-fluid problem studied by Hills (2001). We first solve this linear problem for swirl.

Next, we address the problem for the meridional motion. Since the boundary conditions are uniform, the meridional motion is only driven by the centrifugal force corresponding to term v^2/r in (2.2). This term must be preserved, while the other nonlinear terms can be omitted in the limiting case as $Re \to 0$. Then introducing $u^* = u/Re$ and $w^* = w/Re$ reduces (2.1), (2.2) and (2.4) to

$$r^{-1}\partial(ru^*)/\partial r + \partial w^*/\partial z = 0, \tag{2.8}$$

$$\rho_n \partial p/\partial r - v^2/r = \nu_n(\nabla^2 u^* - u^*/r^2), \tag{2.9}$$

$$\rho_n \partial p/\partial z = \nu_n \nabla^2 w^*. \tag{2.10}$$

The velocity and shear stress components are continuous across the undisturbed interface, $z = H_w$, where the normal-to-interface velocity, w^*, is zero. It is interesting that the entire problem formally is nonlinear despite the motion is creeping, but can be divided into the two linear problems: one for the swirl velocity (2.7) and the other for the meridional motion (2.8)–(2.10). After solving problem (2.7), the 'source' term, v^2/r in (2.9), is prescribed, so the problem for the meridional motion also is linear. This feature is also similar to that in the one-fluid flow studied by Hills (2001).

3. Numerical procedure

To plot flow patterns, it is convenient to transform system (2.8)–(2.10) into the two equations for the Stokes stream function, Ψ, $u^* = -r^{-1}\partial\Psi/\partial z$, $w^* = r^{-1}\partial\Psi/\partial r$, and the azimuthal vorticity component, $\eta = \partial u^*/\partial z - \partial w^*/\partial r$:

$$\nabla^2\Psi - 2r^{-1}\partial\Psi/\partial r = -r\eta, \tag{3.1}$$

$$\nabla^2\eta - (2\partial\eta/\partial r + \eta)/r = -2r^{-1}v\partial v/\partial z. \tag{3.2}$$

First, we solve the linear problem for the swirl velocity (2.7) and the boundary conditions for v. Then, we solve linear equations (3.1) and (3.2) using the obtained solution for v and applying the boundary conditions for Ψ and η which follows from those listed in § 2.3.

The water ($0 < z < H_w$) and air ($H_w < z < 1$) domains are discretized by using a set of n_{zw} and n_{za} Chebyshev spectral collocation points in the axial direction. The radial interval, $0 < r < 1$, is discretized using a set of n_r Chebyshev spectral collocation points. The simulations presented here are done mostly at $n_{zw} = 40$, $n_{za} = 30$ and $n_r = 50$ (standard grid). In order to verify the grid independence of the solution, some runs have been carried out at $n_{zw} = 50$, $n_{za} = 40$ and $n_r = 60$ (fine grid). The comparison of the results obtained with the standard and fine grids can be found in the Appendix.

Since the Chebyshev grid points concentrate near the interface from both sides, the approach is adequate to resolve TCLs, located near the interface, even using moderate values of n_{zw} and n_{za}. The Chebyshev grid points concentrate near the walls as well, that helps to better resolve the Moffatt and other corner eddies. The Chebyshev grid points also concentrate near the axis that helps resolve the vortex breakdown bubble emerging near the axis–bottom intersection as H_w increases.

The discretized problem consists of (i) system of $(n_{zw} + n_{za}) \times n_r$ linear algebraic equations for v and (ii) system of $2(n_{zw} + n_{za}) \times n_r$ linear algebraic equations for Ψ and η. Both systems are solved directly applying the standard procedure of matrix inversion.

https://doi.org/10.1017/jfm.2014.71 Published online by Cambridge University Press

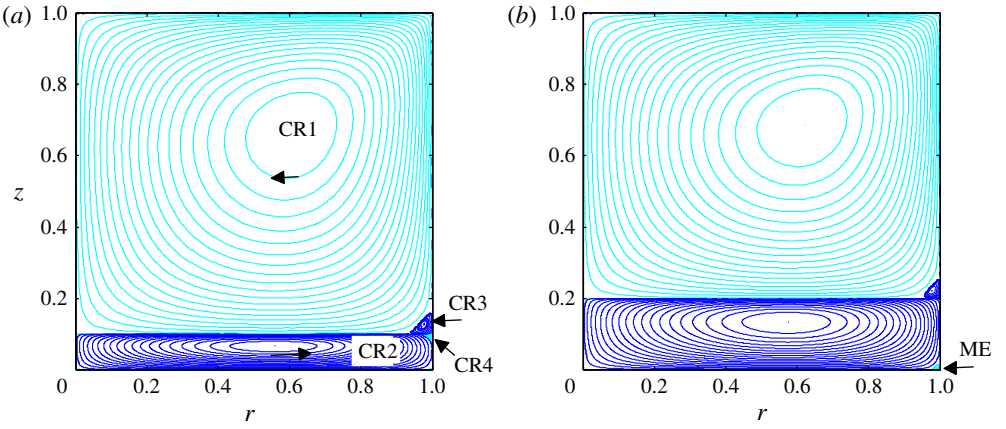


FIGURE 2. (Colour online) Streamlines of meridional flow at H_w = 0.1 (a) and 0.2 (b).

4. Shallow water spout

The flow topology is illustrated by streamlines of the meridional motion, which are contours $\Psi = constant$; Ψ is the Stokes stream function. In the online version of the paper, streamlines have light (deep) blue colour for the clockwise (anticlockwise) motion.

Figure 2 depicts streamline patterns in a shallow water spout at $H_w = 0.1$ (a) and $H_w = 0.2$ (b). The physical reasoning for this flow configuration is that the centrifugal force, induced by the rotating top disk, pushes air to the periphery near the disk and develops the clockwise meridional circulation in region CR1 (figure 2a) resulting in the convergence of air toward the axis near the interface most part. Accordingly at the interface, the meridional velocity, $v_t = u^*$ at $z = H_w$, is directed toward the axis, $v_t < 0$, except in a small vicinity of the sidewall, $r = 1$ (figure 3); subscript 't' indicates that v_t is tangential to the interface.

We plot $(v_t/|v_{tm}|)^{1/3}$ in figure 3 to better observe small positive values of v_t near the sidewall; $|v_{tm}|$ is the magnitude of the minimal v_t value. The meridional motion in the $v_t < 0$ interval of the interface (figure 3) entrains adjacent water and thus drives the anticlockwise circulation of water in region CR2 in figure 2(a).

Circulation CR2 induces a set of the Moffatt eddies in water. Only the outmost eddy is resolved by our grid and shown as ME in the right-lower corner of figure 2(b). Moffatt (1964) revealed that a flow in a corner (between two inclined planes with a sufficiently small angle) has an infinite set of eddies whose strength and scale diminish to zero as the edge is approached. Since the outmost eddy size is small compared with the cylinder radius (see ME in figure 2b), the sidewall can be approximated by a tangential plane thus reducing the cylindrical geometry to the corner between orthogonal planes. The corner angle, 90°, is sufficiently small for the Moffatt eddies to occur. Cell ME also exists, but is hardly visible in figure 2(a). This paper does not count as bifurcations the development of the Moffatt corner vortices only and focuses on the development of TCLs.

The direct effect of the centrifugal force is weak for the meridional motion of the shallow water. At the interface, the swirl velocity substantially drops as H_w decreases (see the values in the second column of table 1). In contrast, variations of the maximal

https://doi.org/10.1017/jfm.2014.71 Published online by Cambridge University Press

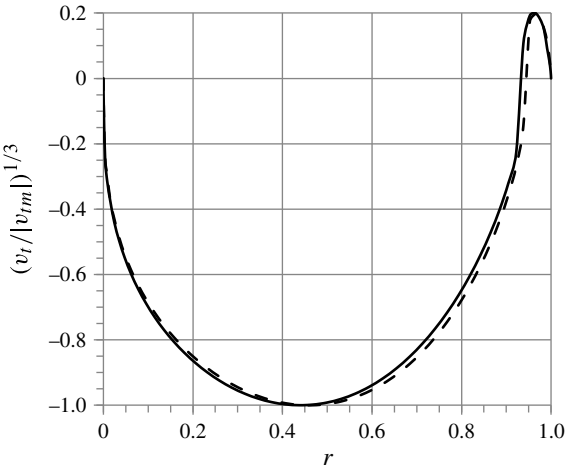


FIGURE 3. Profile of radial velocity at interface v_t normalized by its maximal magnitude, $|v_{tm}|$, at $H_w = 0.1$ (solid curve) and 0.2 (dashed curve).

H_w	v_{max}	v_{tmax}	v_{tmin}
1	1	0	0
0.9	0.03050	8.4239E−06	0
0.8	0.01460	1.306E−06	−5.5401E−08
0.7	0.00877	6.8605E−08	−1.2007E−05
0.6	0.00564	7.7557E−08	−1.3252E−05
0.5	0.00370	8.6092E−08	−1.3467E−05
0.4	0.00239	8.5928E−08	−1.2801E−05
0.3	0.00147	7.9216E−08	−1.1474E−05
0.2	0.00079	7.495E−08	−9.7646E−06
0.1	0.00031	6.3051E−08	−7.9189E−06
0	0	0	0

TABLE 1. Dependence on water volume fraction H_w of the maximal swirl ($v_{\max}$) and radial maximal (v_{tmax}) and minimal (v_{tmin}) velocities at the interface.

magnitude of the radial velocity are small (see the values in the last column of table 1 as H_w varies from 0.1 to 0.7).

The cyclostrophic balance between the centrifugal force and the radial gradient of pressure, $\partial p/\partial r = v^2/r$, typical of high-speed swirling flows, does not work for the water motion at small H_w. Our numerical results at $H_w = 0.2$ show that the maximal value of $\partial p/\partial r$ is around 10 times the maximal value of v^2/r at the interface. Therefore, the contribution of the centrifugal force (see (2.9)) is small to the water meridional motion.

Interesting flow features are cells CR3 and CR4 near the interface–sidewall intersection in figure 2(*a*). Their nature is similar to that of the Moffatt eddies. Since the air-to-water viscosity ratio is small, 0.018, $w = 0$ at $z = H_w$, and u has the second-order zero at $r = 1$, the interface affects the air meridional motions similarly to a horizontal wall does. The $v_t > 0$ range near $r = 1$ in figure 3 corresponds to

https://doi.org/10.1017/jfm.2014.71 Published online by Cambridge University Press

cells CR3 and CR4 in figure 2. The water circulation in CR4 is driven by the air circulation in CR3.

CR3 and CR4 become smaller as H_w increases following the linear relation, $\delta r = 0.071\ (1 - H_w)$, where δr is the radial extent of CR3 and CR4. This relation, extracted from our numerical data, has the following physical reasoning. Denote the flow outside CR3 as SF (source flow). Being driven by the rotating disk, SF decays as z decreases and becomes relatively slow at the interface for small H_w. As H_w increases, SF intensifies near the interface and presses CR3 to the sidewall, diminishing δr down to zero as H_w becomes close to one. In contrast, as H_w decreases down to zero, CR3 becomes the outmost Moffatt eddy. Owing to the small air-to-water dynamic viscosity ratio ($\mu_r = 0.018$), the axial extent of CR4 is smaller than that of CR3 and rapidly shrinks as H_w increases. Even at $H_w = 0.2$, CR4 is too thin to be visible in figure 2(*b*), but CR4 does exist as figure 3 confirms.

The development of the above-described water cells is the first change in the flow topology, as water is added to the air flow. The flow pattern shown in figure 2 remains topologically invariant as the water volume fraction increases up to $H_w = 0.64$. The numerous topological metamorphoses for larger H_w are discussed below.

5. Changes in the flow topology as the water volume increases

5.1. *Development of clockwise circulation near the bottom centre*

Figure 4 depicts streamline patterns at $H_w = 0.64$ (*a*), $H_w = 0.66$ (*b*), 0.68 (*c*) and 0.7 (*d*) illustrating the emergence of circulation region CR5 at $r = z = 0$ and its development as H_w increases. This is an example of corner bifurcation studied by Brøns (1994) and by Brøns (2007). The physical reasoning behind the emergence of region CR5 is discussed below.

As $H_w$increases, the swirl velocity at the interface grows (table 1) and speeds up the rotation of water. This results in that the cyclostrophic balance, $\partial p/\partial r = v^2/r$, becomes nearly established in water (see § 6.4 for more details) except in the bottom vicinity, where the centrifugal force diminishes to the second-order zero due to the no-slip condition, $v = 0$ at $z = 0$. The radial gradient of pressure, being unbalanced by the centrifugal force, pushes water toward the axis and develops the clockwise meridional circulation near the axis–bottom intersection, $r = z = 0$: region CR5 in figure 4(*b*). Interpolating yields that region CR5 emerges at the H_w value which is very close to 0.64. The CR5 emergence is the second change in the flow topology as H_w increases.

5.2. *Merging of near-bottom cells*

As H_w increases, the effect of swirl strengthens, resulting in the expansion of region CR5. First, region CR5 mostly extends in the radial direction and merges with the outmost Moffatt eddy; see ME in figure 4(*b*). This is the third change in the flow topology as H_w increases.

The mergence details are similar to those described by Brøns (2007) and Herrada *et al.* (2013*b*, figure 5): saddle points S_1 and S_2, shown in figure 4(*b*), coalesce into a double saddle point (say, S_4) which separates from the bottom. Region CR2 becomes detached from the bottom and region CR5 becomes extended from the axis up to the sidewall. Next, S_4 merges with the centre of former eddy ME (C_1 in figure 4*b*) and then S_4 and C_1 disappear. Thus, the flow pattern transforms from that shown in figure 4(*b*) into that shown in figure 4(*c*). Further, region CR5 expands upward approaching the interface (figure 4*d*). As region CR5 reaches the interface, the fourth change in the flow topology occurs which is described in detail below.

https://doi.org/10.1017/jfm.2014.71 Published online by Cambridge University Press

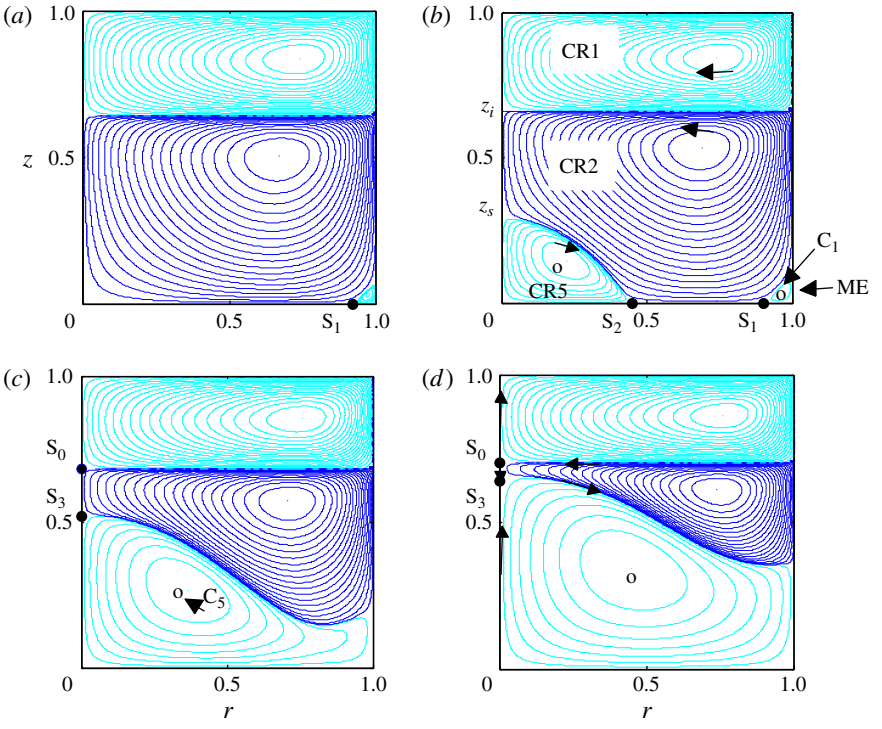


FIGURE 4. (Colour online) Streamline patterns at (*a*) $H_w = 0.64$, (*b*) $H_w = 0.66$, (*c*) $H_w = 0.68$ and (*d*) $H_w = 0.7$.

5.3. *Formation of TCL in air*

Figure 5 depicts the distribution of velocity w^* on the axis, $r = 0$, illustrating the emergence and expansion of region CR5 in the axial direction. We plot $w^{*\,1/3}$ to better observe small w^* near the interface, $z = z_i = H_w$. Table 2 lists values of z_s, corresponding to the boundary between regions CR2 and CR5 (CR1 and CR6) at the axis for $0.64 < H_w < 0.705$ ($0.705 < H_w < 0.905$), and $z_s - z_i$, whose magnitude is the thickness at the axis of region CR2 (figure 4) for $0.64 < H_w < 0.705$ and of region CR6 (figure 6*b*) for $0.705 < H_w < 0.905$.

Figure 8(*a*) schematically shows the flow topology at $H_w = 0.705$. Saddle points S_0 and S_3 (figure 4*c*,*d*) merge into point S_{0m} (figure 8*a*). As increasing H_w passes 0.705, $z_s - z_i$ changes its sign according to table 2. This means that region CR2 separates from the axis topologically transforming from a bubble for $H_w < 0.705$, e.g. as depicted in figure 4(*d*), through a bubble–ring at $H_w = 0.705$ (figure 8*a*) into a ring for $H_w > 0.705$, e.g. as depicted to the right of saddle point S in figure 6. Point S_{0m} (figure 8*a*) splits into saddles S_0 and S_3 shown in figure 8(*b*) and region CR6 emerges (figure 6). This is the fourth change in the flow topology as H_w increases.

For $H_w > 0.705$, the radial velocity at the interface, v_t, reverses near the axis as figure 7 illustrates where $v_t^{1/3}$ is plotted to better observe small positive and negative v_t. In figure 7, v_t changes its sign at $r = r_S$, which is the radial coordinate of saddle point S located on the interface (figure 6). The reversed meridional velocity at the interface (intervals $v_t > 0$ in figure 7) drives adjacent air away from the axis and thus develops a thin layer of anticlockwise air circulation: region CR6 in figure 6.

https://doi.org/10.1017/jfm.2014.71 Published online by Cambridge University Press

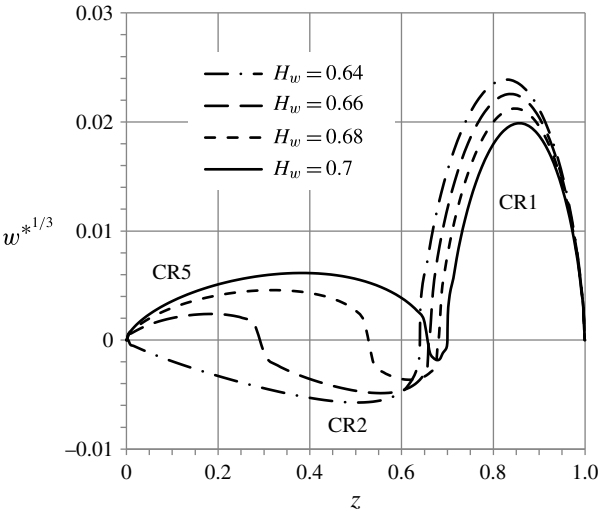


FIGURE 5. Profiles of velocity w^* on the axis at $H_w = 0.64$, 0.66, 0.68 and 0.7 show the emergence and development of region CR5 (figure 4).

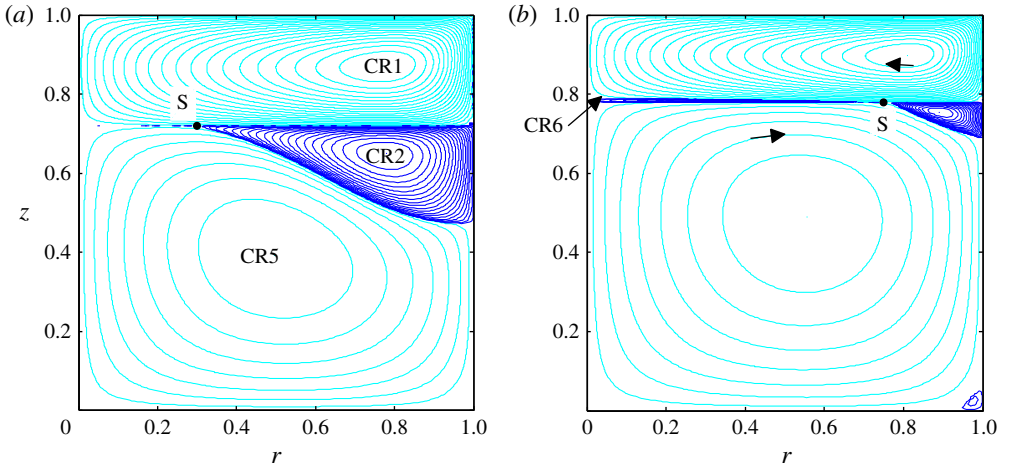


FIGURE 6. (Colour online) Streamline patterns at (*a*) $H_w = 0.72$ and (*b*) $H_w = 0.78$.

Region CR6 is well observed in figure 6(*b*) extending from the axis up to saddle point S. Although region CR6 is so thin at $H_w = 0.72$ that is hardly visible in figure 6(*a*), its existence follow from the $v_t > 0$ part of curve $H_w = 0.72$ in figure 7. Figure 8(*b*) schematically shows the shape and structure of region CR6 at $H_w = 0.72$ (figure 6*a*). CR6 has one inner stagnation point (centre) shown by a small circle in figure 8(*b*).

5.4. *Emergence of a RBR*

An interesting feature, documented in table 2, is that the thickness of layer CR6, $z_s - z_i$, is not a monotonic function of H_w: first $z_s - z_i$ increases with H_w, reaches its local maximum near $H_w = 0.72$, then drops down to zero, and remains to be zero in the range $0.745 < H_w < 0.785$.

https://doi.org/10.1017/jfm.2014.71 Published online by Cambridge University Press

$H_w = z_i$	z_s	$z_s - z_i$
0.64	0	−0.64
0.66	0.29	−0.37
0.68	0.525	−0.155
0.7	0.659	−0.041
0.705	0.705	0
0.725	0.724	0.0054
0.74	0.7432	0.0032
0.745	0.745	0
0.785	0.785	0
0.8	0.812	0.012
0.82	0.839	0.019
0.84	0.869	0.029
0.86	0.904	0.044
0.88	0.947	0.067
0.905	1	0.095

TABLE 2. Dependence on water volume fraction H_w of z_s (figure 4*b*) and thickness, $|z_s - z_i|$, of regions CR2 (for $H_w < 0.705$) and CR6 (for $H_w > 0.705$) at the axis.

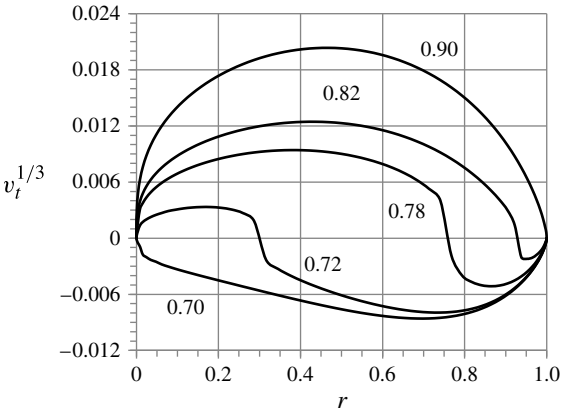


FIGURE 7. Profiles of meridional velocity v_t at the interface at H_w values shown near the curves.

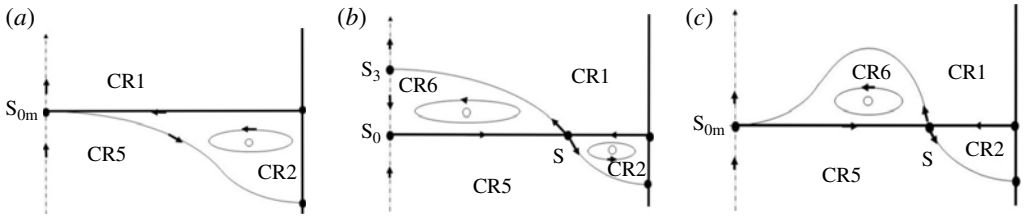


FIGURE 8. Schematics of flow patterns at (*a*) $H_w = 0.705$, (*b*) $H_w = 0.72$ and (*c*) $H_w = 0.78$.

This range, where the CR6 thickness is zero at the axis, is referred to as the RBR range below. Figure 9 depicts the dependence of $z_s - z_i$ on H_w. The dashed curves

https://doi.org/10.1017/jfm.2014.71 Published online by Cambridge University Press

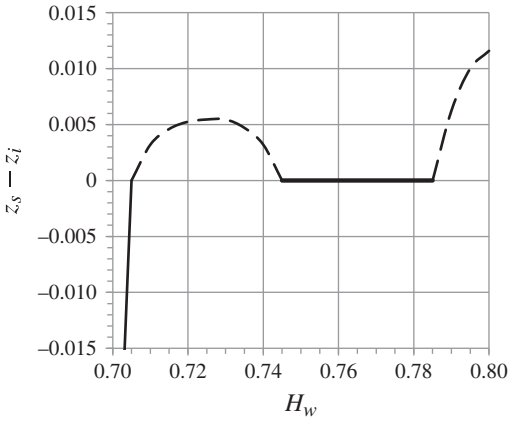


FIGURE 9. Dependence of $z_s - z_i$ on H_w shows the RBR range (bold line).

show positive $z_s - z_i$, the thin solid curve shows negative $z_s - z_i$, and the bold solid line shows the RBR range where $z_s - z_i = 0$. The derivative, $\mathrm{d}(z_s - z_i)/\mathrm{d}H_w$, has jumps at the RBR boundaries and at $H_w = 0.705$ where $z_s - z_i$ changes its sign. These jumps are due to the different properties of air and water.

The increasing $z_s - z_i$ changes its sign at $H_w = 0.705$ because the water flow can easily reverse the air flow. In contrast, the air flow cannot easily reverse the water flow. Accordingly, when the decreasing $z_s - z_i$ reaches zero at $H_w = 0.745$, it does not become negative, remaining to be zero up to $H_w = 0.785$, where $z_s - z_i$ begins to increase, as figure 9 illustrates.

In the RBR range, CR6 does not separate from the axis (CR6 corresponds to intervals $0 < r < r_s$ where $v_t > 0$ in figure 7), touching it at the single point, where the axis and interface intersect, as figure 8(*c*) schematically shows.

Therefore, our simulations with very high yet finite numerical accuracy indicate that CR6 topologically is a RBR in the RBR range. The transformation of region CR6 from a bubble (figure 8*b*) into a bubble–ring (figure 8*c*) is the fifth change in the flow topology as H_w increases.

The bubble–ring shape is typically transitional between the bubble and the ring shapes. A small variation of a control parameter (here H_w) transforms a bubble–ring into a bubble or into a ring. For example, such generic metamorphosis occurs as increasing H_w passes 0.705 (table 2): region CR2 topologically is a bubble for $H_w < 0.705$ (figure 4*d*), a bubble–ring at $H_w = 0.705$ (figure 8*c*) and a ring for $H_w > 0.705$ (figure 6).

First, RBRs were found in the $Re \gg 1$ whirlpool flow (Herrada, Shtern & López-Herrera 2013*c*). Our paper reveals RBR in the $Re \ll 1$ water-spout flow. The common feature is that all of these RBRs are attached to and exist due to the interface.

Figure 10 depicts the distribution of velocity w^* on the axis, $r = 0$, at $H_w = 0.78$, i.e. within the RBR range. Curve $w^*(z)$ touches line $w^* = 0$ at $z = z_i = H_w$, but there is no tangency. The derivative, $\partial w^*/\partial z$, is not zero and changes its sign by a jump at $z = z_i$. The jump, following from condition (2.5), is due to the different densities and viscosities of air and water. The jump can occur only at the interface, $z = z_i$, and $\partial w^*/\partial z$ is a smooth function for $z < z_i$ and $z > z_i$. The local minimum of $w^*(z)$ with a jump in $\partial w^*/\partial z$ is a specific feature of the RBR occurrence: compare the w^* profiles at $H_w = 0.7$ (figure 5), $H_w = 0.78$ (figure 10) and $H_w = 0.8$ (figure 15).

https://doi.org/10.1017/jfm.2014.71 Published online by Cambridge University Press

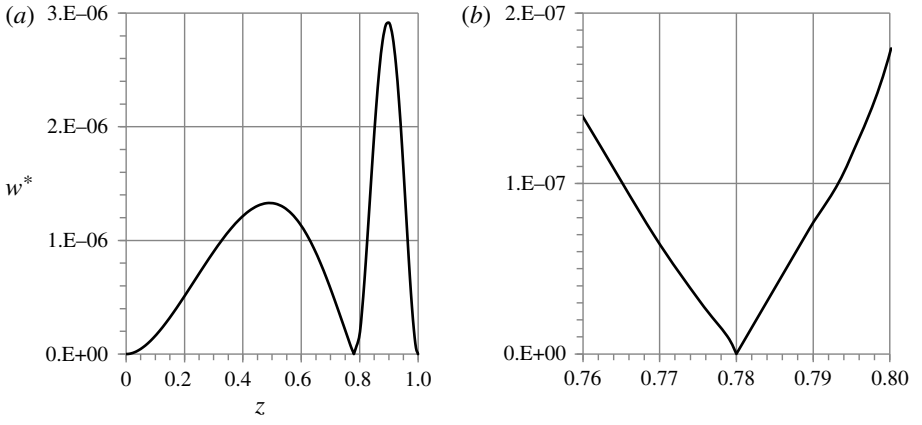


FIGURE 10. (*a*) Profile of velocity w^* at the axis at $H_w = 0.78$, (*b*) close up of (*a*) near $z = H_w$.

5.5. *Disappearance of the RBR*

According to table 2 and figure 9, $z_s - z_i$, again becomes positive, as increasing H_w passes $H_w = 0.785$. This means that region CR6 transforms back from the bubble–ring shape (figure 8*c*) into the bubble shape (figure 8*b*). This is the sixth change in the flow topology as H_w increases. Now we analyse the most-cellular flow (taking $H_w = 0.8$ as an example) in more detail.

6. Deep water spout at $H_w = 0.8$

6.1. *Streamline pattern*

Figure 11 depicts the streamline pattern at $H_w = 0.8$. It is striking that this creeping flow has so many cells observed in figure 11: circulation regions CR1, CR3 and CR6 in air, circulation regions CR2, CR5 and the Moffatt eddy ME in water.

The two clockwise circulations, in regions CR1 and CR5, have opposite directions near the interface in figure 11. This counterflow affects the near-interface motion. Near $r = 1$, the air circulation, CR1, dominates, drives a small amount of water away from the sidewall and thus generates region CR2 with the anticlockwise circulation. Near the axis, the water circulation, CR5, dominates, drives a thin layer of air away from the axis, and thus generates region CR6 with the anticlockwise circulation. Figure 11(*b*) depicts CR6 and its vicinity enlarged in the z direction. Note that region CR3 is visible in figure 11(*b*) as well.

6.2. *Meridional velocity at the interface*

Figure 12 helps better understand this multicell pattern by depicting the profile of meridional velocity, v_t, at the interface. The maximal value of v_t is $v_{tm} = 1.31 \times 10^{-6}$ at $H_w = 0.8$. Figure 12 depicts $(v_t/v_{tm})^{1/3}$ to better observe small v_t near the sidewall and reveals that v_t is positive in interval $0 < r < r_S = 0.852$ and negative in interval $r_S < r < 1$. The positive v_t is due to the water circulation in region CR5 (figure 11). On the other hand, according to the clockwise circulation in region CR1, air moves toward the axis near the interface, i.e. in the opposite direction to the interface velocity in range $0 < r < r_S$. This counterflow constitutes a thin layer of anticlockwise circulation in air region CR6 (figure 11).

https://doi.org/10.1017/jfm.2014.71 Published online by Cambridge University Press

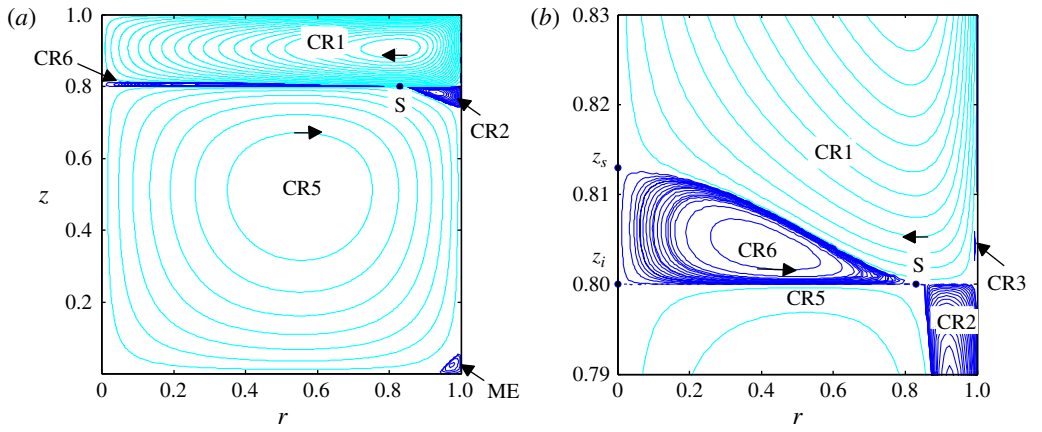


FIGURE 11. (Colour online) (*a*) Streamlines of the meridional motion at $H_w = 0.8$; (*b*) close up of CR6.

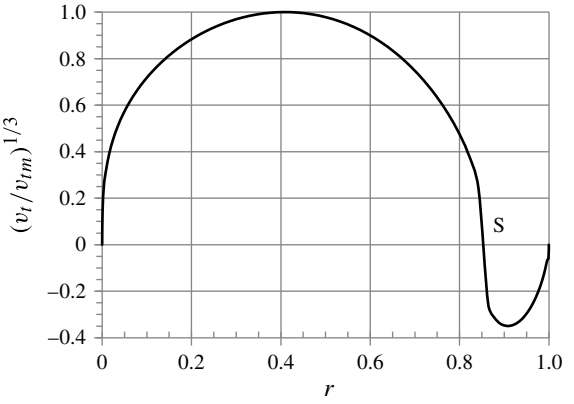


FIGURE 12. Profile of meridional velocity at interface at $H_w = 0.8$.

The negative v_t in range $r_S < r < 1$ (figure 12) is a co-flow with the clockwise circulation in region CR1 (figure 11). In a swirl-free flow, the clockwise circulation of air in region CR1 would drive the anticlockwise circulation of water. Such circulation does occur near the sidewall in region CR2 in figure 11 where the swirl velocity diminishes to zero at the sidewall due to the no-slip condition, $v = 0$ at $r = 0$.

6.3. *Swirl velocity at the interface*

Figure 13 depicts the profile of swirl velocity v at the interface. The friction at the sidewall and viscous diffusion significantly reduces maximal swirl velocity at interface to $v_m = 0.0146$ at $H_w = 0.8$ from the maximal swirl velocity at the top disk which is one. However, v_m is about 10^4 times v_{tm}. This dominance of the swirl velocity over the radial velocity causes that the centrifugal force drives water near-interface to periphery except in the sidewall vicinity where the effect of the clockwise circulation (CR1) of air dominates the effect of the centrifugal force.

Based on the above analysis, we conclude that regions CR1, CR2, CR5 and CR6 meet at the saddle point S, $r = r_S$ and $z = 0.8$, as figure 8(*b*) schematically depicts.

https://doi.org/10.1017/jfm.2014.71 Published online by Cambridge University Press

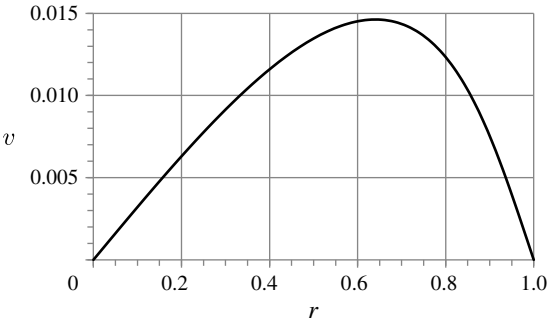


FIGURE 13. Profile of swirl velocity on interface at $H_w = 0.8$.

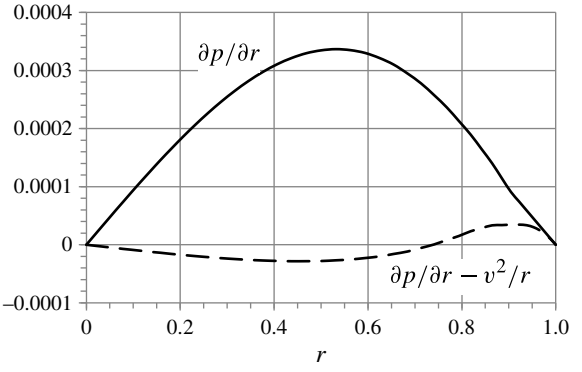


FIGURE 14. Distribution of $\partial p/\partial r$ and $\partial p/\partial r - v^2/r$ at the interface at $H_w = 0.8$.

There the bold horizontal (vertical) line denotes the interface (sidewall). The thin curve separates regions CR1 and CR6 (CR2 and CR5) above (below) the interface. The dot-dashed line is the axis of rotation and the arrows indicate the flow direction. Saddle point S is shown in figures 8, 11 (the bold point) and 12.

6.4. *Cyclostrophic balance at the interface*

Figure 14 helps explain, why the meridional motion is so weak compared with swirl, by depicting the radial gradient of pressure ($\partial p/\partial r$, solid curve) and the left-hand side of (2.9) for the water flow (dashed curve) at the interface. Comparison of the solid and dashed curves in figure 14 reveals that centrifugal force is mostly compensated by the pressure gradient, i.e. the cyclostrophic balance, $\partial p/\partial r = v^2/r$ typical of high-speed swirling flows, works in this creeping motion as well. The difference, $\partial p/\partial r - v^2/r$, drives the interface radial flow to the periphery near the axis, $r = 0$, and toward the axis near the sidewall, $r = 1$, as the dashed curve illustrates in figure 14.

6.5. *Velocity at the axis*

For the air motion, the water-flow feedback is weak compared with the direct driving by the rotating disk. This explains why the layer of anticlockwise circulation of air (region CR6 in figure 11) is so thin compared with the large domain of air clockwise circulation (region CR1 in figure 11).

https://doi.org/10.1017/jfm.2014.71 Published online by Cambridge University Press

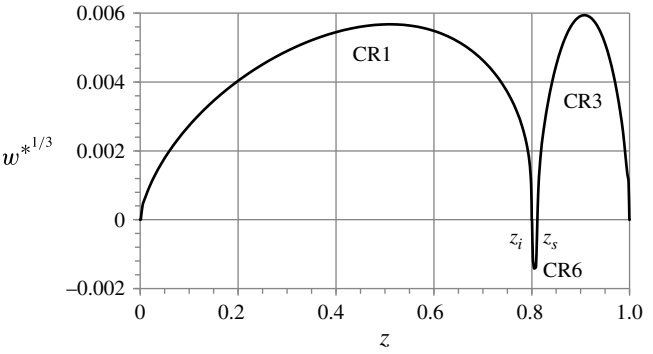


FIGURE 15. Profile of velocity at axis at $H_w = 0.8$. The $w^* < 0$ range corresponds to region CR6 in figure 11.

H_w	0.705	0.72	0.74	0.76	0.78	0.8	0.82	0.84	0.8425
r_S	0	0.297	0.517	0.569	0.675	0.852	0.926	0.992	1

TABLE 3. Radial length r_S of region CR6 versus water volume fraction H_w.

Figure 15 depicts the profile of velocity w^* along the axis. We plot $w^{*1/3}$ to better observe w^* in the small interval, $0.8 = z_i < z < z_s = 0.812$ where $w^* < 0$, which corresponds to region CR6 in figure 11. The thickness of region CR6 at the axis, 0.012, is very small compared with its length, $r_S = 0.853$. The maximal magnitude of w^* in interval $z_i < z < z_s$ is very small compared with that in interval $z_s < z < 1$. This indicates that the meridional motion in region CR6 is very slow compared with that in region CR1 (see figure 11). Figure 15 also shows that the maximal velocities at the axis are close for the air and water flows. As H_w further increases approaching one, all air cells disappear as described below.

7. Collapse of air cells

7.1. *Extension of the TCL up to the sidewall*

Table 3 lists the radial coordinate, r_S, of saddle point S (figure 11), which is the length of layer CR6, versus H_w. According to table 3, region CR6 emerges at $H_w = 0.705$, extends as H_w increases, and reaches the sidewall at $H_w = 0.8425$. For $H_w > 0.8425$, region CR6 spreads from the axis up to the sidewall and region CR1 becomes separated from the interface as table 3 indicates and figure 16 depicts. This is a corner-crossing bifurcation Brøns (2007) and the seventh change in the flow topology as H_w increases.

7.2. *Extension of region CR6 up to the top disk*

As H_w increases, region CR6 expands in the axial direction as well and reaches the top disk at $H_w = 0.905$ according to table 2. Therefore, region CR1 becomes separated from the axis for $H_w > 0.905$ (figure 17*a*). This is the eighth change in the flow topology.

Figure 17 illustrates how region CR1 shrinks and disappears as H_w approaches one. The saddle point S_t located at the top disk (figure 17*a*) is the upper point of the

https://doi.org/10.1017/jfm.2014.71 Published online by Cambridge University Press

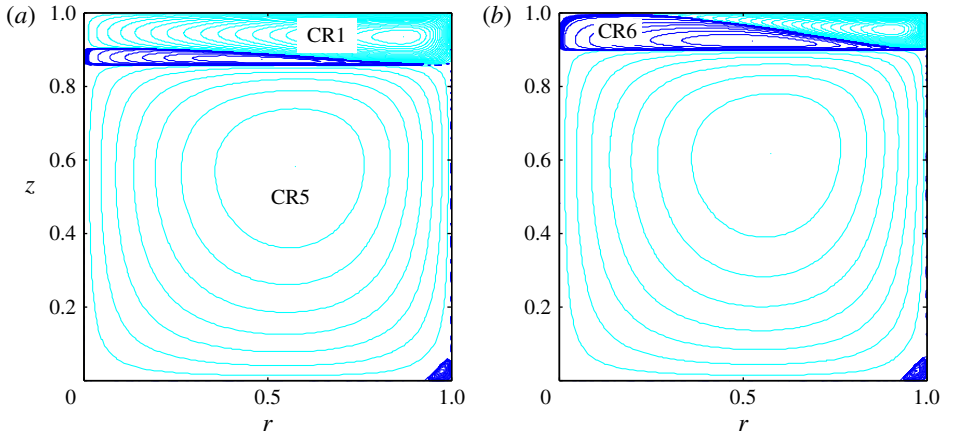


FIGURE 16. (Colour online) Streamline patterns at (*a*) $H_w = 0.86$ and (*b*) $H_w = 0.9$.

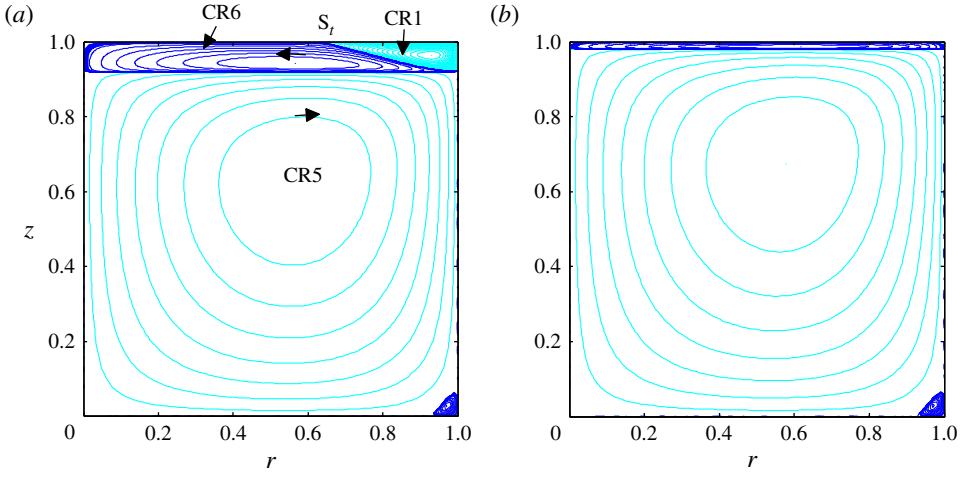


FIGURE 17. (Colour online) Streamline patterns at (*a*) $H_w = 0.92$ and (*b*) $H_w = 0.98$.

boundary between regions CR1 and CR6. Its radial coordinate, r_t, as a function of H_w is listed in table 4.

Interpolating data in table 4 yields that region CR1 disappears at $H_w = 0.987$. This is the ninth change in the flow topology. Finally, region CR6 disappears at $H_w = 1$.

Table 4 also shows how the maximal swirl velocity at the interface, v_{max}, grows with H_w. Even at $H_w = 0.98$, v_{max} is still seven times smaller than its limiting value, 1, as $H_w \to 1$. An interesting feature is that the maximal radial velocity at the interface, v_{tmax}, increases with H_w up to $H_w = 0.98$ despite v_{tmax} must drop to zero at $H_w = 1$. Therefore, a very thin layer of air can remarkably change the flow characteristics near the top disk.

8. The effect of the air-to-water density ratio

Now we explore how the air-to-water density ratio affects the flow topology. To this end, we increase pressure inside the cylindrical container at a fixed (room)

https://doi.org/10.1017/jfm.2014.71 Published online by Cambridge University Press

H_w	0.9	0.92	0.94	0.96	0.98	1
r_t	0.132	0.642	0.823	0.928	0.982	1
v_{max}	0.0305	0.0380	0.0501	0.0729	0.1327	1
v_{tmax}	8.42E−06	1.31E−05	2.24E−05	4.48E−05	1.25E−04	0

TABLE 4. Radial extent, r_t, of region CR6 at the top disk (figure 16) and the maximal swirl (v_{max}) and meridional (v_{tmax}) velocities at the interface versus water volume fraction H_w.

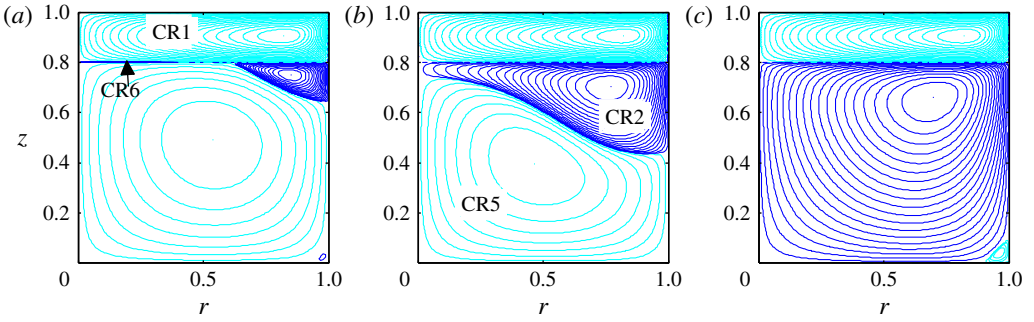


FIGURE 18. (Colour online) Changes in the flow pattern as the air density increases (*a*) two, (*b*) four and (*c*) eight times that used in figure 11.

temperature T. According to the ideal gas relation, $\rho_a = p/(R_g T)$, air density ρ_a is proportionally to pressure p; R_g is the gas constant. Since the air dynamic viscosity, $\mu_a = \rho_a \nu_a$, only depends on T, μ_a is invariant as p changes. The water properties also remain unchanged. Therefore, as ρ_a increases to $a\rho_a$, $\nu_n = \nu_a/\nu_w$ and $\rho_n = \rho_w/\rho_a$ decrease to ν_n/a and ρ_n/a, respectively, while μ_r stays invariant; $a > 1$ is the amplifying factor. We fix $H_w = 0.8$ and increase the air density by doubling a. Figure 11 depicts the flow pattern at $a = 1$, and figure 18 depicts the flow patterns at $a = 2$ (*a*), 4 (*b*) and 8 (*c*).

The numerical results depicted in figure 18 reveal that the effect of the increasing air density is similar to that of the decreasing water volume: first, region CR6 shrinks and region CR2 expands (figure 18*a*, compare with figure 6*a*); second, region CR6 disappears and region CR2 extends from the sidewall up to axis (figure 18*b*, compare with figure 4*d*); and third, region CR5 shrinks and disappears (figure 18*c*), The flow pattern depicted in figure 18(*c*) topologically is identical to the patterns depicted in figure 2. As the air density further increases, the flow topology, shown in figure 18(*c*), does not change.

The physical reasoning behind this trend is the following. The distribution of swirl velocity does not depend on the densities of both fluids. It follows from (2.7) and the boundary conditions for v. In contrast, the meridional motion does depend on the densities of the fluids. As the air density increases, the air meridional circulation (in region CR1 in figure 18) speeds up. Table 5 shows that the air maximal velocity at the axis, w^*_{amax}, increases nearly proportional to the density amplifying factor, a.

Accordingly, for the water motion, the effect of the air circulation strengthens and finally overcomes the effect of the centrifugal force, as ρ_a grows (figure 18). The

https://doi.org/10.1017/jfm.2014.71 Published online by Cambridge University Press

a	1	2	4	8
$w^*_{amax} \times 10^6$	2.09	4.49	9.31	19.96

TABLE 5. The maximal velocity of air at the axis versus density amplifying factor a.

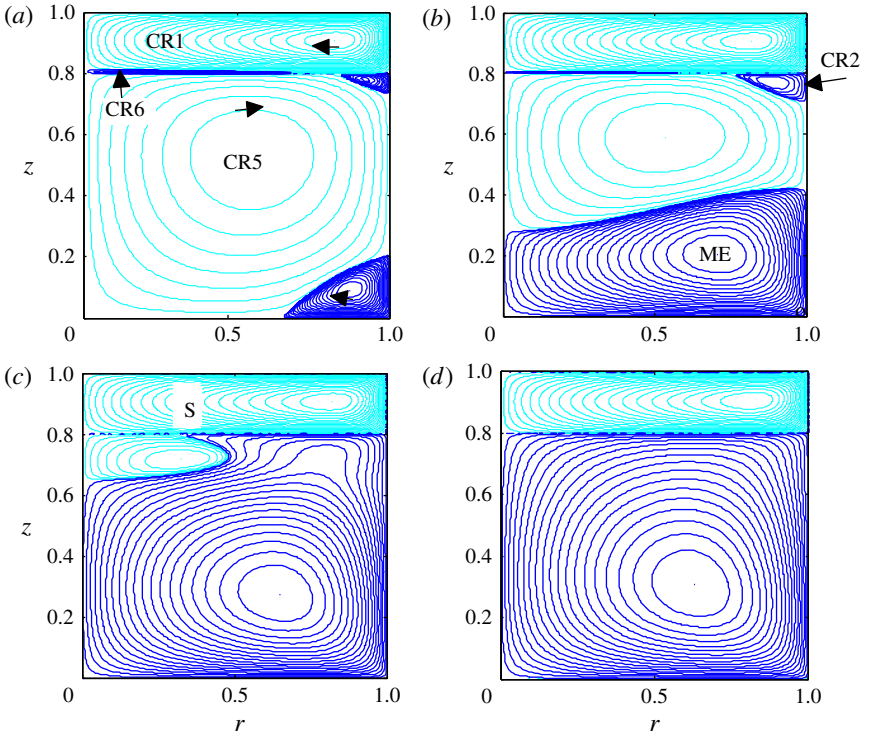


FIGURE 19. (Colour online) Changes in the flow pattern (shown in figure 11) as the rotation of the bottom disk speeds up: (*a*) $\alpha = 0.01$, (*b*) $\alpha = 0.02$, (*c*) $\alpha = 0.03$ and (*d*) $\alpha = 0.04$; see conditions (9.1).

nature of the effect of increasing volume fraction of air, as H_w decreases, is similar to that as ρ_a grows. Based on these results, we conclude that the multicell pattern shown in figure 11 occurs due to the small air-to-water density ratio (0.00122).

9. The pattern control by the bottom disk co-rotation

The flow pattern can be controlled by additional co-rotation of the bottom disk. To show this, we change the boundary conditions for the swirl velocity at the top and bottom disks to

$$v = \alpha r \quad \text{at } z = 0 \quad \text{and} \quad v = (1-\alpha) r \quad \text{at } z = H. \tag{9.1}$$

Figure 19 depicts how the flow pattern, shown in figure 11 where $\alpha = 0$, changes at $\alpha = 0.01$ (*a*), 0.02 (*b*), 0.03 (*c*) and 0.04 (*d*). As α further increases, the flow topology remains the same as that at $\alpha = 0.04$ (figure 19*d*).

https://doi.org/10.1017/jfm.2014.71 Published online by Cambridge University Press

The effect of increasing α is the most prominent near the sidewall where the centrifugal force is maximal, pushes water to the periphery and drives the anticlockwise circulation. This results in the expansion of the outmost Moffatt eddy (ME in figure 19*a*,*b*). The strengthening anticlockwise circulation weakens the clockwise circulation in region CR5 that causes the expansion of cell CR2 and shrinking of layer CR6 (figure 19*a*).

First, region ME predominantly expands in the radial direction, reaches the axis, and detaches region CR5 from the bottom (figure 19*b*). Next, ME and CR2 merge and detach region CR5 from the sidewall (figure 19*c*). At α value between 0.02 and 0.025, the thickness of layer CR6 at the axis drops to zero and CR6 topologically becomes a bubble–ring. At $\alpha = 0.03$, regions CR1, CR2, CR6 and ME meet at saddle point S in figure 19(*c*). Finally, regions CR2 and CR6 shrink and collapse at the axis–interface intersection, and the flow pattern (figure 19*d*) becomes similar to that shown in figure 2.

The flow topology has been studied above for creeping flows. Now we investigate in what range of Re, the flow topology remains the same as that for $Re \ll 1$.

10. The effect of increasing rotation of the top disk

To explore the effect of finite values of the Reynolds number, we come back from the reduced problem (§ 2.4) to the full problem (§§ 2.2 and 2.3) and use the numerical techniques described in detail by Herrada *et al.* (2013*a*). The key features are: (i) mapping of both the air and water regions onto the fixed rectangular domain and (ii) using the Chebyshev grid. This allows us to resolve TCL even with a moderate number of grid points.

For finite Re, the interface becomes deformed. The deformation depends on the Froude number, $Fr = \omega^2 R/g = aRe^2$, and the Weber number, $We = \rho_w \omega^2 R^3/\sigma = bRe^2$; $a = \nu_w^2/(gR^3)$ and $b = \rho_w \nu_w^2/(R\sigma)$. We fix a and b while increase Re. The bioreactor radius, R, is around 0.02 m (Liow *et al.* 2009) or larger (Ramazanov *et al.* 2007); this yields $a = 1.25 \times 10^{-8}$, and $b = 7 \times 10^{-7}$. For the range $Re < 800$ considered here, Fr, We and the interface deformation are small.

It is reasonable to characterize the water-spout flow by the Reynolds number based on the air viscosity, $Re_a = \omega R^2/\nu_a = Re/\nu_n$, because the rotating top disk directly (indirectly) drives the air (water) flow. While increasing Re_a, we fix $H_w = 0.8$ and $\rho_a = 1.22$ kg m^{-3}.

Figure 20 depicts the streamline patterns at $Re_a = 200$ (*a*), 600 (*b*) and 800 (*c*). At $Re_a = 200$ (figure 20*a*), the flow topology is the same as in the creeping flow (figure 11). The quantitative difference is that the thickness at the axis, $z_s - z_i$, and the length in the radial direction, r_S, of layer CR6 as well as the maximal swirl velocity at the interface, v_{max}, become smaller at $Re_a = 200$ than those for $Re_a \ll 1$ (table 6).

The first change in the flow topology occurs as increasing Re_a passes $Re_1 = 314$: the axial thickness of layer CR6, $z_s - z_i$, becomes zero (table 6), i.e. layer CR6 topologically transforms from a bubble (figure 8*b*) into a bubble–ring (figure 8*c*). This is a minor topological change: compare figure 20(*a*) and figure 20(*b*) where the CR6 transformation is not visible.

The second change in the flow topology occurs as Re_a passes $Re_2 = 568$: the range $v_t > 0$ disappears at the interface, the radial length of layer CR6, r_S, diminishes to zero (table 6), i.e. layer CR6 collapses while region CR2 becomes extended from the sidewall to the axis (figure 20*c*).

https://doi.org/10.1017/jfm.2014.71 Published online by Cambridge University Press

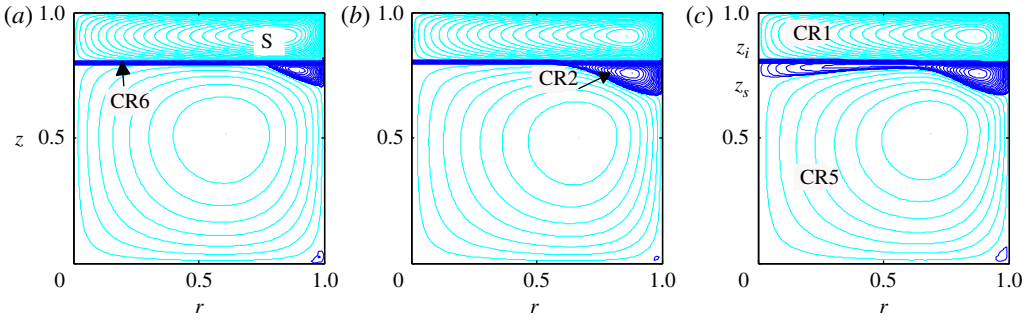


FIGURE 20. (Colour online) Streamline patterns at $H_w = 0.8$ and (*a*) $Re_a = 200$, (*b*) $Re_a = 600$ and (*c*) $Re_a = 800$.

Re_a	z_s	$z_s - z_i$	r_S	v_{max}	v_{tmax}	v_{tmin}
$Re_a \ll 1$	0.8116	0.0116	0.852	0.0146		
133	0.8047	0.0047	0.789	0.0134	0.00120	−0.00022
200	0.8025	0.0025	0.745	0.0128	0.00103	−0.00045
267	0.801	0.0010	0.704	0.0123	0.00079	−0.00072
$Re_1 = 314$	0.8	0	0.678	0.0119	0.00057	−0.00100
533	0.8	0	0.528	0.0111	0.00005	−0.00168
$Re_2 = 568$	0.8	0	0	0.0111	0	−0.00175
600	0.786	−0.005	0	0.0111	0	−0.00182
800	0.736	−0.064	0	0.0111	0	−0.00222

TABLE 6. The axial coordinate, z_s, and its difference with that of the interface, $z_s - z_i$, for the boundary between regions of clockwise and anticlockwise circulations (figure 18*c*), the radial coordinate of saddle point S (figure 18*a*), r_S, the maximal swirl, v_{max}, maximal meridional, v_{tmax}, and minimal meridional, v_{tmin}, velocities at the interface versus the Reynolds number, Re_a.

As figure 20(*c*) depicts, the axial thickness of region CR2 is minimal in the middle between the axis and the sidewall at $Re_a = 800$. Our numerical simulations reveal that region CR2 splits into its near-axis and near-sidewall parts as Re_a increases. However for large Re, the flow becomes unstable. One-fluid flows in a sealed cylinder become unstable for $Re > 3000$ (Gelfgat, Bar-Yoseph & Solan 2001). We expect that two-fluid flows become unstable at smaller Re than that for one-fluid flows. For this reason our simulations are limited here to $Re_a < 800$.

The results of this section at $H_w = 0.8$ and the prior results at $H_w = 0.5$ (Herrada *et al.* 2013*b*) indicate that the flow pattern of the creeping air–water flow remains topologically invariant as Re_a increases up to a few hundred.

11. Conclusions

Our numerical simulations describe a slow air–water flow, driven by the top rotating disk, in a sealed vertical cylinder of aspect ratio $H = 1$. As water volume fraction H_w increases from 0 to 1, the nine changes in the flow topology occur, listed in table 7.

https://doi.org/10.1017/jfm.2014.71 Published online by Cambridge University Press

N	H_w	Topology change	Figure
1	0.64	Region CR5 emerges	4(*b*)
2	0.67	Region CR2 separates from the bottom	4(*c*)
3	0.675	Saddle and centre merge in CR5	4(*c*)
4	0.705	Region CR2 separates from the axis Region CR6 emerges as a bubble	6(*a*)
5	0.745	Region CR6 becomes a RBR	6(*b*) and 8(*c*)
6	0.785	Region CR6 becomes a bubble	11 and 8(*b*)
7	0.8425	Region CR1 separates from the interface	16
8	0.905	Region CR1 separates from the axis	17(*a*)
9	0.9847	Region CR1 disappears	17(*b*)

TABLE 7. List of the flow topology changes as water volume fraction H_w grows.

The flow pattern is multicellular at H_w around 0.8 (figure 11). The revealed mechanism of the cell formation differs from that in one-fluid creeping flows. Here, the mechanism is kinematic: (i) the rotating top disk drives the clockwise meridional circulation of adjacent air, (ii) the air swirl and meridional motions compete in the development of the clockwise and anticlockwise circulations in water and (iii) the clockwise circulation of water provides feedback driving a thin layer of the anticlockwise circulation in air.

The multicell pattern occurs due to the small value of the air-to-water density ratio. As this ratio increases (with increasing pressure inside the container), two cells disappear (CR5 and CR6 in figure 18). The flow pattern can be controlled by additional rotation of the bottom disk. Even a weak co-rotation suppresses the clockwise (anticlockwise) circulation in water (air) as figure 19 illustrates.

The creeping flow topology remains invariant in a moderately fast flow: up to $Re_a = 314$ (figure 20*a* and table 6). At $Re_a = 800$, there are two bulk regions of the clockwise meridional circulation, one in air and the other in water, separated by a thin water layer adjacent to the entire interface, where the meridional circulation is anticlockwise (figure 20*c*).

The obtained results are of fundamental interest and can be useful for applications, e.g. bioreactors.

Acknowledgements

Partial support from the Ministry of Science and Education and Junta de Andalucía (Spain) through Grants No. DPI2010-21103 and No. TEP-7465, respectively, is gratefully acknowledged.

Appendix

Figure 21 helps compare the numerical data obtained with the standard (crosses) and fine grids (see § 3) for the creeping flow at $H_w = 0.8$ described in § 6. The data for swirl (figure 21*a*) and radial (figure 21*b*) velocities at the interface, $z = H_w$, coincide with the accuracy of the drawing in figure 21. This coincidence being the most valuable for the radial velocity, v_t, which is very small (especially near the sidewall, $r = 1$, where $v_t < 0$), confirms the grid convergence of the results reported in this paper.

https://doi.org/10.1017/jfm.2014.71 Published online by Cambridge University Press

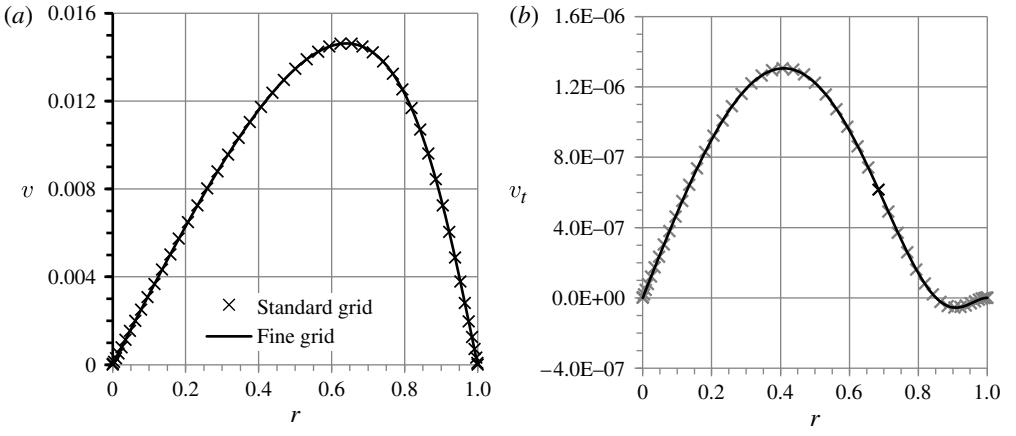


FIGURE 21. Distributions of (*a*) swirl, v, and (*b*) meridional, v_t, velocities at the interface at $H_w = 0.8$ (figure 10) obtained with the standard (crosses) and fine (solid curves) grids.

REFERENCES

BATCHELOR, G. K. 1967 *An Introduction to Fluid Dynamics*. Cambridge University Press.

BLAKE, J. 1979 On the generation of viscous toroidal eddies in a cylinder. *J. Fluid Mech.* **95**, 209–222.

BRADY, P. T., HERMAN, M. & LOPEZ, J. M. 2012*a* Two-fluid confined flow in a cylinder driven by a rotating end wall. *Phys. Rev.* E **85**, 016306.

BRADY, P. T., HERMAN, M. & LOPEZ, J. M. 2012*b* Addendum to 'Two-fluid confined flow in a cylinder driven by a rotating end wall'. *Phys. Rev.* E **85**, 067301.

BRØNS, M. 1994 Topological fluid dynamics of interfacial flows. *Phys. Fluids* **6**, 2730–2737.

BRØNS, M. 2007 Streamline topology: patterns in fluid flows and their bifurcations. *Adv. Appl. Mech.* **41**, 1–42.

BRØNS, M., VOIGT, L. K. & SØRENSEN, J. N. 2001 Topology of vortex breakdown bubbles in a cylinder with a rotating bottom and a free surface. *J. Fluid Mech.* **428**, 133–148.

GELFGAT, A. YU., BAR-YOSEPH, P. Z. & SOLAN, A. 2001 Three-dimensional instability of axisymmetric flow in a rotating lid cylinder enclosure. *J. Fluid Mech.* **438**, 363–377.

GÜRCAN, F., GASKELL, P. H., SAVAGE, M. D. & WILSON, M. C. T. 2003 Eddy genesis and transformations of Stokes flow in a double-lid driven cavity. *Proc. Inst. Mech. Engrs* C **217**, 353–364.

HALL, O., HILLS, C. P. & GILBERT, A. D. 2007 Slow flow between concentric cones. *Q. J. Mech. Appl. Maths.* **60**, 27–48.

HAPPEL, J. R. & BRENNER, H. 1965 *Low Reynolds number hydrodynamics*. Springer.

HERRADA, M. A., SHTERN, V. N. & LÓPEZ-HERRERA, J. M. 2013*a* Off-axis vortex breakdown in a shallow whirlpool. *Phys. Rev.* E **87**, 063016.

HERRADA, M. A., SHTERN, V. N. & LÓPEZ-HERRERA, J. M. 2013*b* Vortex breakdown in a water-spout flow. *Phys. Fluids* **25**, 093604.

HERRADA, M. A., SHTERN, V. N. & LÓPEZ-HERRERA, J. M. 2013*c* Bubble-ring cells in a whirlpool flow. Manuscript submitted in *Phys. Rev. E*.

HILLS, C. P. 2001 Eddies induced in cylindrical containers by a rotating end wall. *Phys. Fluids* **13**, 2279–2286.

LIOW, K. Y. S., TAN, B. T., THOUAS, G. & THOMPSON, M. C. 2009 CFD modeling of the steady-state momentum and oxygen transport in a bioreactor that is driven by a rotating disk. *Mod. Phys. Lett.* B **23** (2), 121–127.

LO JACONO, D., NAZARINIA, M. & BRØNS, M. 2009 Experimental vortex breakdown topology in a cylinder with a free surface. *Phys. Fluids* **21**, 111704.

https://doi.org/10.1017/jfm.2014.71 Published online by Cambridge University Press

MOFFATT, H. K. 1964 Viscous and resistive eddies near a sharp corner. *J. Fluid Mech.* **18**, 1–18.

RAMAZANOV, YU. A., KISLYKH, V.I., KOSYUK, I. P., BAKULEVA, N. V. & SHCHURIKHINA, V. V. 2007 Industrial production of vaccines using embryonic cells in gas-vortex gradient-less bioreactors. In *New Aspects of Biotechnology and Medicine* (ed. A. M. Egorov), pp. 87–91.

SHANKAR, P. N. & DESHPANDE, M. D. 2000 Fluid mechanics in the driven cavity. *Annu. Rev. Fluid Mech.* **32**, 93–136.

SHTERN, V. 2012*a* A flow in the depth of infinite annular cylindrical cavity. *J. Fluid Mech.* **711**, 667–680.

SHTERN, V. 2012*b* *Counterflows*. Cambridge University Press.

WAKIYA, S. 1976 Axisymmetric flow of a viscous fluid near the vertex of a body. *J. Fluid Mech.* **78**, 737–747.

WILSON, M. C. T., GASKELL, P. H. & SAVAGE, M. D. 2005 Nested separatrices in simple shear flows: the effect of localized disturbances on stagnation lines. *Phys. Fluids* **17**, 093601.

https://doi.org/10.1017/jfm.2014.71 Published online by Cambridge University Press